

See discussions, stats, and author profiles for this publication at: <https://www.researchgate.net/publication/281203217>

# Quasi Core/Shell Lead Sulfide/Graphene Quantum Dots for Bulk Heterojunction Solar Cells

ARTICLE *in* THE JOURNAL OF PHYSICAL CHEMISTRY C · AUGUST 2015

Impact Factor: 4.77 · DOI: 10.1021/acs.jpcc.5b04195

---

CITATION

1

READS

86

## 5 AUTHORS, INCLUDING:



[mohammad mahdi tavakoli](#)  
Sharif University of Technology

20 PUBLICATIONS 32 CITATIONS

[SEE PROFILE](#)



[A. Simchi](#)  
Sharif University of Technology

197 PUBLICATIONS 3,529 CITATIONS

[SEE PROFILE](#)



[Sergii Kalytchuk](#)  
Palacký University of Olomouc

39 PUBLICATIONS 203 CITATIONS

[SEE PROFILE](#)



[Zhiyong Fan](#)  
The Hong Kong University of Science and Tec...

118 PUBLICATIONS 6,199 CITATIONS

[SEE PROFILE](#)

# Quasi Core/Shell Lead Sulfide/Graphene Quantum Dots for Bulk Heterojunction Solar Cells

Mohammad Mahdi Tavakoli,<sup>†,‡</sup> Hossein Aashuri,<sup>†</sup> Abdolreza Simchi,<sup>\*,†,§</sup> Sergii Kalytchuk,<sup>||</sup> and Zhiyong Fan<sup>‡</sup>

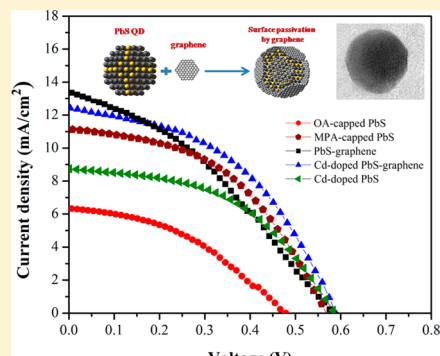
<sup>†</sup>Department of Materials Science and Engineering and <sup>§</sup>Institute for Nanoscience and Nanotechnology, Sharif University of Technology, 14588 Tehran, Iran

<sup>‡</sup>Department of Electronic and Computer Engineering, Hong Kong University of Science and Technology, Clear Water Bay, Kowloon, Hong Kong

<sup>||</sup>Department of Physics and Materials Science & Centre for Functional Photonics (CFP), City University of Hong Kong, Hong Kong SAR

## S Supporting Information

**ABSTRACT:** Hybrid nanostructures combining semiconductor quantum dots and graphene are attracting increasing attention because of their optoelectronic properties promising for photovoltaic applications. We present a hot-injection synthesis of a colloidal nanostructure which we define as quasi core/shell PbS/graphene quantum dots due to the incomplete passivation of PbS surfaces with an ultrathin layer of graphene. Simulation by density functional theory of a prototypical model of a nonstoichiometric Pb-rich core (400 atoms) coated by graphene (20 atoms for each graphene sheet) indicates the possibility of surface passivation of (111) planes of PbS with graphene resulting in a decrease in trap states and recombination sites. The graphene coating of the PbS quantum dots decreases the exciton lifetime up to  $0.78\ \mu\text{s}$  as compared to  $1.2\ \mu\text{s}$  for the oleic acid passivated PbS quantum dots due to the fast extraction of carriers. We have employed PbS/graphene as well as Cd-doped PbS/graphene quantum dots as active layers of bulk heterojunction solar cells, and we achieved solar power conversion efficiencies of 3.6 and 4.1%, respectively.



## 1. INTRODUCTION

Semiconductor quantum dots (QDs) have emerged as attractive choices for low-cost, solution processed optoelectronic devices, such as lasers, diodes, and solar cells, due to their photostability, high charge carrier mobility, and band gap tunability upon appropriate surface treatment.<sup>1–3</sup> Of particular interest, PbS QDs can be synthesized from earth-abundant elements, while their band gap can easily be size-tuned over a broad spectral range extending into the near-infrared.<sup>4,5</sup> Owing to these useful properties, the interest in the field of PbS QD photovoltaics has surged, prompted by the observation that short conjugated ligands of the nanocrystals can increase the carrier mobility in thin films by several orders of magnitude. The transportation of charge carriers within QD solids crucially depends on the distance between QDs which is determined by their surface ligands, as well as by the existence of midgap and shallow states associated with imperfect and disorder QD surfaces.<sup>6,7</sup> Various approaches toward QD film formation utilized different types of chemical reagents for the surface treatment of QDs to form highly conductive QD arrays.<sup>8–10</sup> Further improvements have been achieved by atomic-ligand passivation<sup>11–13</sup> and construction of quantum junction devices.<sup>14,15</sup> Recently, a record solar conversion performance of 8.55% has been reported for PbS QD solar cells using a solid-

state ligand exchange, wherein the long-chain ligand oleic acid (OA) commonly used in QD synthesis has been replaced with 1,2-ethanedithiol.<sup>16</sup>

In recent years, many useful electronic, optical, and mechanical properties of graphene (G) have been highlighted for photovoltaic applications,<sup>17–19</sup> such as high electron mobility ( $15\ 000\ \text{cm}^2/\text{V}\cdot\text{s}$ ),<sup>20–22</sup> low production cost, and extremely large surface area ( $\sim 2600\ \text{m}^2/\text{g}$ ).<sup>23–26</sup> Hybrid heterostructures where graphene is combined with semiconductor nanocrystals are attracting increasing attention as promising candidates for optoelectronic devices and sensors.<sup>27–31</sup> Konstantatos et al.<sup>32</sup> introduced hybrid PbS/G photodetectors consisting of a ultrahigh thin film graphene covered with a thin film of colloidal PbS QDs, with an ultrahigh gain ( $\sim 10^8$  electrons per photoanode responsivity of  $\sim 10^7\ \text{A}/\text{W}$ ). Huang et al.<sup>33</sup> studied the photoresponse of hybrid PbS/G film deposited on an n-type silicon substrate covered by a thin  $\text{SiO}_2$  layer, and observed considerable changes in the resistance of the graphene channel under irradiation with a laser beam. Zhang et al.<sup>27</sup> fabricated single-layer graphene transistors by

Received: May 1, 2015

Revised: July 24, 2015

Published: July 27, 2015

chemical vapor deposition method, and demonstrated their improved sensitivity to light upon deposition of PbS films with different thicknesses by electron beam thermal evaporation. Parand et al.<sup>34</sup> employed PbS/G nanocomposites as a counter electrode in CdS/CdSe QD sensitized solar cells, which were grown by *in situ* deposition of PbS QDs on graphene sheets using the SILAR method.

In the present work, we introduce a solution-based hot-injection method to synthesize monodisperse PbS/G QDs of a quasi core/shell type, due to the incomplete passivation of PbS surfaces with an ultrathin layer of graphene. The lifetime of charge carriers is decreased in the PbS/G QDs as compared with organic ligand capped PbS QDs. The ultrathin layer of graphene also passivates the surface trap states of PbS QDs while decreasing the spacing between the adjacent nanocrystals in the QD films. This allowed us to utilize PbS/G QDs as well as Cd-doped PbS/G QDs as thin active layers of bulk heterojunction solar cells, with solar conversion efficiencies (PCEs) of 3.6 and 4.1%, respectively.

## 2. EXPERIMENTAL SECTION

**2.1. Materials.** Lead(II) oxide powder (PbO, 99%), oleic acid (OA, technical grade 90%), anhydrous toluene, octane, methanol, isopropyl alcohol, and Triton X-100 were purchased from Merck, Germany. Bis(trimethylsilyl) sulfide (TMS, Strem, 97% purity), 3-mercaptopropionic acid (MPA, Sigma-Aldrich, ≥99% purity), 1-octadecene (ODE, Sigma-Aldrich, technical grade 90%), titanium diisopropoxide bis(acetylacetone) solution (75% in 2-propanol, Sigma-Aldrich), and titanium tetrachloride (Sigma-Aldrich) were used as received without further purification.

**2.2. Synthesis of Reduced Graphene Oxide.** Graphene oxide (GO) dots were synthesized by electrolysis of a graphite rod<sup>35</sup> which was performed on a CHI 705 power supply (CHInstruments, China) with a current density of 120 mA/cm for 20 min. The graphite rod anode was inserted into 7 mL of aqueous solution of NaOH (0.1 M), and a Pt foil was employed as a counter electrode. The obtained solution after electrolysis was centrifuged at 10 000 rpm for 10 min in order to remove the insoluble residuals. The GO dots were converted into reduced graphene oxide (rGO) dots by supercritical fluid ethanol and using a reactor with a capacity of 30 mL.<sup>36</sup> GO dots and ethanol were mixed to achieve a concentration of 0.3 mg/mL, and the pH was adjusted to 5.7 by the use of NaOH. The reaction vessel was heated quickly (30 °C/min) to 330 °C and held at this temperature for 20 min, with the pressure maintained at 38–40 MPa. Afterward, the vessel was removed from the furnace and quenched in a cold water bath (~5 °C) to decrease the temperature quickly. The resulting rGO with an average diameter of 2.5 nm and high purity (*Supporting Information, Figure S1*) was separated by centrifugation (4000 rpm), washed several times by ethanol, and redispersed in ODE (120 mg/mL).

**2.3. Synthesis of PbS/Graphene Quantum Dots.** One milliliter of rGO dots solution in ODE (0.1 mg/mL) and 0.45 g of PbO were mixed with 3 mL of ODE and maintained in a flask at 110 °C for 16 h. After the addition of 15 mL of ODE to the flask, a solution containing 210 μL of TMS dissolved in 10 mL of ODE was swiftly injected and the PbS/G QDs were nucleated from the solution in less than 1 s. The reaction product was separated by centrifugation (4000 rpm), followed by several times washing with methanol and acetone, and finally redispersed in octane.

For the Cd doping of PbS/G QDs, we adapted a chemical procedure similar to common procedure for the treatment of PbS QDs.<sup>12–15</sup> A 0.1 g sample of TDPA, 2 mmol of CdCl<sub>2</sub>, and 10 mL of oleylamine were mixed in a flask at 100 °C for 30 min to obtain a transparent light-yellow solution. Twelve milliliters of the octane solution of PbS/G QDs (80 mg/mL) was mixed with 4 mL of this Cd-containing solution and maintained for 2 h, followed by washing and redispersion of the resulted QDs in octane. OA-capped PbS QDs were also synthesized by the hot-injection method, as explained in detail in ref 11.

**2.4. Device Fabrication.** Commercial FTO substrates with ohmic sheet resistance of 8 Ω were obtained from Lumtec, Taiwan. They were cleaned by immersion in deionized (DI) water (Millipore, 18 MΩ·cm) containing 3 vol % Triton X-100 and sonicated for 30 min, rinsed with water, sonicated in 2-propanol for 30 min and in DI water for 30 min, and finally dried under nitrogen flow. A mesoporous TiO<sub>2</sub> layer composed of 20 nm sized particles was spin-coated on FTO glasses at 4000 rpm for 45 s using a TiO<sub>2</sub> paste (Dyesol 18NRT, Dyesol) dispersed in ethanol. After drying at 125 °C, the TiO<sub>2</sub> films were annealed at 500 °C for 30 min and cooled to room temperature followed by TiCl<sub>4</sub> treatment as previously reported.<sup>37</sup> Bulk heterojunction solar cells were fabricated by deposition of colloidal solutions of QDs (80 mg/mL) in octane on TiO<sub>2</sub> substrates by spin-coating (2500 rpm). In order to replace the long OA ligand with short thiol molecules of MPA, a solid-state ligand exchange process was afforded. Herein, after deposition of the PbS QDs by spin-coating at 2500 rpm for 30 s, a MPA solution (1 vol % in anhydrous methanol) was spread on the surface for 3 s, spin-cast (2500 rpm) for 10 s, and finally washed by anhydrous methanol twice. This process was repeated for 10 runs until a uniform film of ~300 nm thickness was attained. The films were dried in a nitrogen-filled glovebox, and the top contact MoO<sub>3</sub>/Au layers were thermally evaporated at a rate of ~0.8 Å/s.

**2.5. Materials Characterization.** A high-resolution transmission electron microscope (HRTEM, JOL, JEM-2100, Japan) equipped with energy-dispersive X-ray spectroscopy (EDS) was employed for structural studies. X-ray diffraction (XRD, Stone Sandi P, USA) utilizing Cu Kα radiation was used for phase characterization. Infrared spectra were recorded on a PerkinElmer Fourier transform infrared spectrometer (FTIR, Spectrum RX, USA). An InVia (Renishaw AB, Sweden) spectrometer using incident laser light with 514.5 nm wavelength was employed to record Raman spectra. X-ray photoelectron spectroscopy (XPS) was measured using a hemispherical analyzer with an Al Kα X-ray source (1486.6 eV) at 10<sup>-7</sup> Pa. Gaussian components after a Shirley background subtraction were employed for peak deconvolution and analysis of XPS data. Optical absorption was studied on a Varian Cary 500 spectrometer (Varian, USA). Photoluminescence (PL) spectra were recorded on an FLS920P fluorescence spectrometer (Edinburgh Instruments) equipped with a cryogenically cooled photomultiplier (R5509-43, Hamamatsu), with an excitation source for steady-state spectra with a 450 W continuous xenon arc lamp and a picosecond pulsed diode laser (EPL-405, excitation wavelength 405 nm, pulse width 49 ps) for lifetime measurements. PL decay curves were obtained using fitting a stretched exponential function  $I(t) = I_0 e^{-(t/\tau)^\beta}$ , where  $\tau$  is the decay time and  $\beta$  is a stretch parameter. The photoluminescence quantum yield (PLQY) was measured by an absolute method using the same fluorescence spectrometer

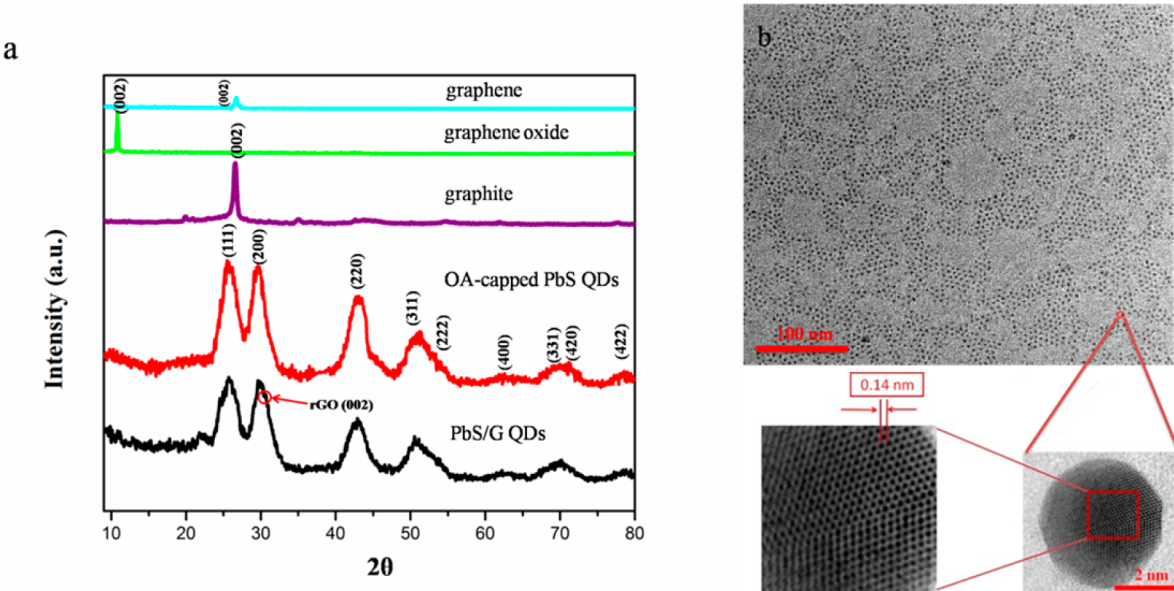


**Figure 1.** (a) XRD patterns of PbS/G and OA-capped PbS QDs as compared to graphitic materials, indicating that nanocrystals are composed of cubic crystals of PbS and graphene. (b) HRTEM images of hybrid PbS/G QDs show that ultrafine crystals ( $\sim 3.5$  nm) are capped with an ultrathin layer of GQDs.

equipped with an integrating sphere with BENFLECR coated inner face (Edinburgh Instruments). The spectral correction curve which into account the sensitivity of the monochromator, detector, sphere coating, and optics to wavelength was provided by Edinburgh Instruments. The thickness, morphology, and roughness of the samples were evaluated by field-emission scanning electron microscopy (FESEM, Hitachi S4160, Japan).

**2.6. Photovoltaic Performance of Solar Cells.** The solar spectrum at AM1.5G was simulated with a Xe lamp using filters with an intensity of  $100 \text{ mW cm}^{-2}$ . The current density–voltage ( $J-V$ ) data were obtained using a Keithley 2400 (USA) instrument.  $J-V$  sweeps were scanned between  $-1$  and  $+1$  V using a delay time of 150 ms at each point and a step size of 0.02 V. External quantum efficiency (EQE) spectra were measured using a white light bias with  $5 \text{ mW cm}^{-2}$  intensity provided by an array of white light-emitting diodes. The excitation beam was generated by xenon lamp with a 300 W (ILC Technology) and the signal was obtained by using an Amplifier (Model SR830 DSP Lock-In).

**2.7. Density Function Theory Simulation.** The electronic structure of the hybrid PbS/G structure compared to nonpassivated PbS QDs was studied by density functional theory (DFT). Simulations were performed on a prototypical model of a nonstoichiometric Pb-rich 2.4 nm PbS QD core (400 atoms) and graphene (20 atoms for each graphene sheet). SIESTA-3.2 software was used for DFT simulations based on numerical atomic orbitals as a basis, scalar-relativistic Troullier–Martins pseudopotentials, and the generalized gradient approximation (GGA) with PBE96 as exchange-correlation function. In order to optimize the geometry, the forces on the atoms were controlled until they converged to below 40 meV/A. The energy cutoff used was 200 Ry. A Monkhorst–Pack method was also used for the  $k$ -point choices.

### 3. RESULTS AND DISCUSSION

XRD patterns of PbS/G and OA-capped PbS QDs are presented in Figure 1a in comparison with those for graphite,

graphene oxide, and rGO. Diffraction peaks corresponding to both PbS and rGO are observed in the PbS/G QDs pattern, with those for PbS fitting well with the cubic lead sulfide (JCPDS 02-0699). The main characteristic peak of graphene appears at  $26^\circ$  ( $d$ -spacing of 0.34 nm), indicating the presence of graphene in these QDs.<sup>20</sup> Nevertheless, it should be noted that this peak may be overlapped with the peak of (111) planes of QDs. It is also evident that the ultrathin layer of graphene decreases the peak intensity of PbS QDs while making it more broadened.

The TEM image of PbS/G QDs shown in Figure 1b indicates nanocrystals with an average size of 3.5 nm and narrow size distribution. TEM image, selected area electron diffraction (SAED), and EDS analysis data for PbS/G QDs are shown in Figures S2 and S3. The interplanar spacing of PbS QDs is 0.295 nm, which indicates the distance between two (200) planes of the cubic PbS phase. The average diameter of OA-capped PbS QDs is 3 nm, slightly smaller than those for the PbS/G QDs. HRTEM analysis of PbS/G nanocrystals confirms that the layer surrounding the PbS QDs could be an ultrathin layer of graphene due to its hexagonal structure and the distance of 0.14 nm between carbon atoms (Figure 1b), which agree well with the graphene structure.<sup>38</sup> In this case, the crystalline planes of the particular PbS QD did not properly align with respect to the electron beam to get clear lattice fringes while the graphene layer did, and as a result, it was possible to resolve the graphene layer only. In Figure 2, we introduce two models for other possibilities. Here, the PbS fringes are overlapped with the graphene lattice. In Figure 2a, the HRTEM images of PbS/G QDs look very different from those of the isolated graphene dots (see Figure S1). The spacing of lattice fringes in those images is found to be 0.10–0.11 nm, which corresponds to the carbon fringes of graphene as schematically shown in Figure 2b. On the other hand, no lattice fringe which corresponds to PbS is observed. A possible reason is that the  $d$  spacing of the (111) and (200) planes of PbS crystal are 0.34 and 0.296 nm, respectively, and thus, the

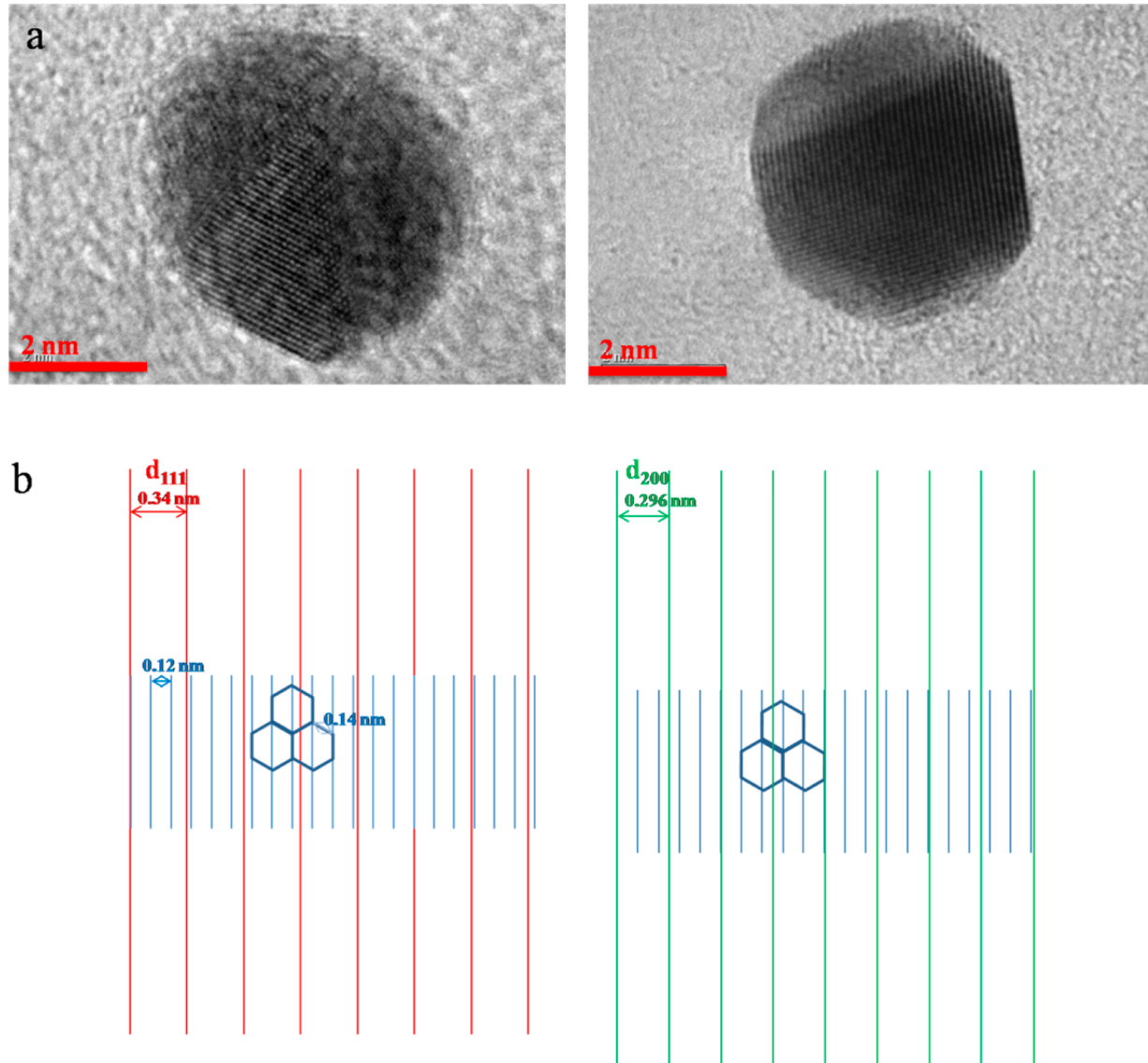


**Figure 2.** (a) HRTEM images of PbS/G QDs and (b) models of crystalline structure of PbS/G QDs in which are shown overlapping of PbS fringes with the graphene lattice.

number of planes in such a small QD is less than 10 even if the PbS is a single crystal. The mean crystalline size of PbS estimated from XRD peaks is about 3 nm, and thus, the number of planes could be less than 10. In addition, if an ultrathin layer of graphene attaches on the PbS crystal surface aligning its direction with the PbS crystal orientation, fringes of both graphene and PbS overlap each other to some extent as illustrated in Figure 2b. Because the fringe spacing of PbS is much larger than that of graphene, no more patterns will be observed. Those may be the reasons why no PbS lattice fringe is observed in the HRTEM images while graphene fringe could be clearly observed. Similar results were observed for Cd-doped PbS/G QDs, as illustrated in Figure S4.

Figure 3a shows FTIR spectra of rGO, OA-capped PbS, and PbS/G QDs. The FTIR spectrum of rGO illustrates the broad peak of O–H groups located at  $3534.59\text{ cm}^{-1}$ , the  $1726.1\text{ cm}^{-1}$  peak coming from the bending vibration of C=O groups, and C–H stretching at  $2850$  and  $2922\text{ cm}^{-1}$ .<sup>27</sup> The peak at  $1627.64\text{ cm}^{-1}$  is assigned to the skeleton vibration of graphitic domains (C=C band). The FTIR spectrum of OA-capped PbS

nanocrystals has two peaks around  $1398$  and  $1528\text{ cm}^{-1}$  and two others near  $2849$  and  $2918\text{ cm}^{-1}$ , which are ascribed to the carboxyl group and CH<sub>2</sub> bonds of the oleic acid ligand, respectively.<sup>38</sup> The FTIR spectrum of PbS/G QDs shows that the peak intensity was reduced as compared with rGO.

Figure 3b shows Raman spectra of the PbS/G QDs as compared with those for graphene oxide, graphite, and reduced graphene oxide. Graphite illustrates a peak at  $1578.5\text{ cm}^{-1}$  (G band), which is related to the vibration of sp<sup>2</sup>-bonded carbon in the hexagonal structure.<sup>18</sup> Compared with pristine graphite, for GO the G-band peak is upshifted ( $1588.5\text{ cm}^{-1}$ ) because of the existence of isolated double bonds which resonate at frequencies higher than that of the G-band of the graphite.<sup>28</sup> The presence of D-band at  $1320\text{ cm}^{-1}$  points out the existence of defects and disorders in graphitic sheets imposed by highly oxidizing conditions. As shown in Figure 3b, the D band of GO, rGO, and PbS/G QDs becomes broader and stronger due to the higher level of disorder of the graphene layers, resulting in an increase in the  $I_D/I_G$  ratio. As shown in Figure 3b, graphite

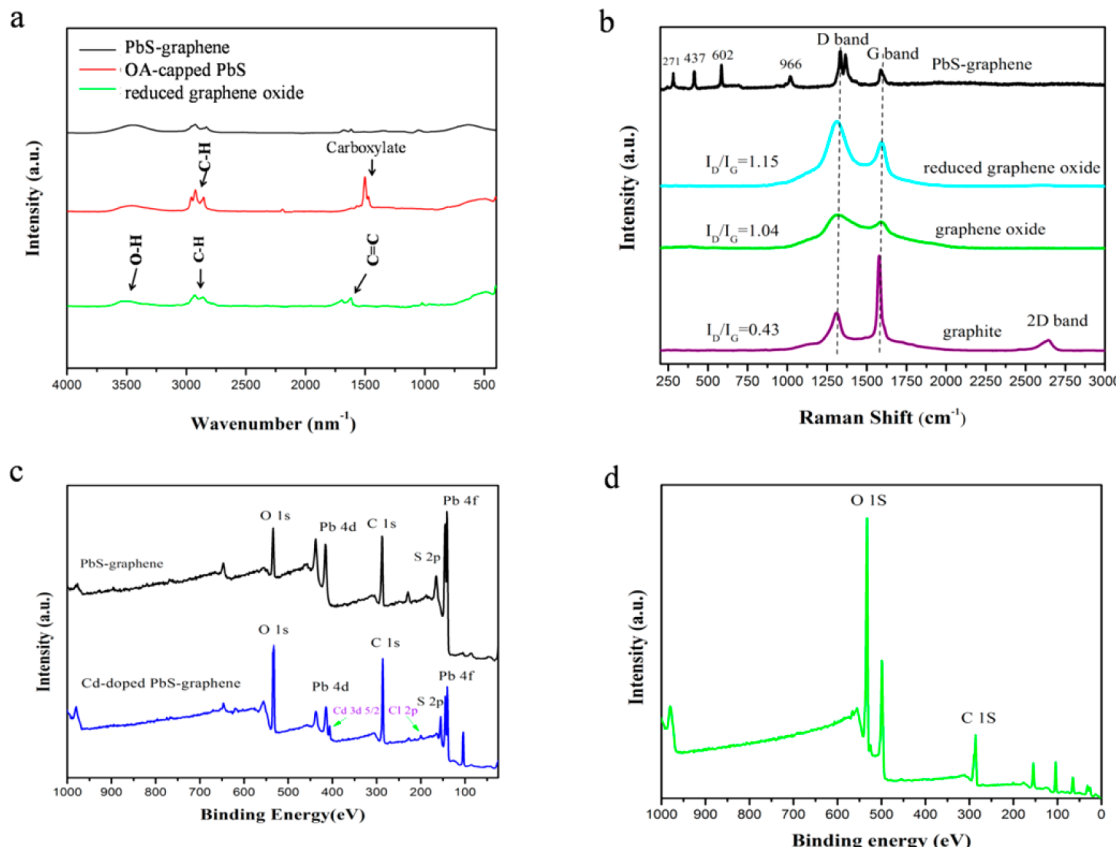


**Figure 3.** Spectroscopic characterization of PbS/G QDs and GO using (a) FTIR and (b) Raman spectroscopies. XPS spectra of (c) PbS/G QDs and (d) GO.

shows a peak at  $2668\text{ cm}^{-1}$  (2D band), which is not seen in the corresponding spectrum of GO, rGO, and PbS/G QDs.

As shown in Figure 3b, the peak at  $271\text{ cm}^{-1}$  for PbS/G QDs is related to the surface phonon mode.<sup>18</sup> The peaks at  $437$  and  $602\text{ cm}^{-1}$  are from 2LO and 3LO phonon modes (longitudinal optical phonons) of PbS/G QDs, respectively. The weak peak at  $966\text{ cm}^{-1}$  may be related to the photodegradation of PbS.<sup>18</sup> The double degenerate D peak divided into two sub-bands, including  $D^+$  ( $1356.7\text{ cm}^{-1}$ ) and  $D^-$  ( $1320.1\text{ cm}^{-1}$ ), but this did not occur for the G peak. This phenomenon most probably originated from the strain induced symmetry breaking, with polarization along and perpendicular to the strain.<sup>38</sup> This can be related to strain induced due to the bending of the graphene layer on the surface of PbS QDs.

X-ray photoelectron spectroscopy (XPS) was employed to study the composition of the PbS/G and Cd-doped PbS/G QDs. It indicates that functional groups of GO were reduced during the supercritical ethanol, and the Cd doping was successfully performed. The XPS spectrum of PbS/G (Figure 3c) shows the predominant graphitic C 1s peak at  $285\text{ eV}$ , an O 1s peak at  $534\text{ eV}$ , S 2p at  $165\text{ eV}$ , and Pb 4d and 4f at  $416$  and  $141\text{ eV}$ , respectively. Two new peaks, Cd 3d<sub>5/2</sub> and Cl 2p, appear at  $406.4$  and  $199.6\text{ eV}$ , respectively, as a result of Cd doping of the PbS/G nanocrystals.<sup>37</sup> The weaker O 1s peak of PbS/G QD relative to the corresponding C 1s peak and O 1s peak of GO (Figure 3d) indicates that the reduction of GO has taken place after supercritical ethanol. High-resolution XPS spectra of C 1s of PbS/G and GO (Figure S5) show that the intensity of the C–O peak is lower in the PbS/G QDs as compared to GO. The peaks are also slightly shifted to higher

energies. Therefore, it can be concluded that the most of the oxygen-containing functional groups of GO are reduced after reduction at the surface of PbS QDs. According to the DFT simulation results, most of the atoms on the surface of PbS QDs are Pb atoms due to the nonstoichiometric structure of a PbS QD. The XPS and FTIR results show that rGO still has the C–O functional group on its surface. Based on these data, it is feasible to suggest the following mechanism of formation of quasi core/shell PbS/G structure.  $\text{Pb}^{2+}$  ions chemisorbed at the nucleating PbS crystals react with functional groups on the surface of rGO, leading to formation of  $\text{Pb}–\text{O}–\text{C}$  bonds. Furthermore, a layer-by-layer chemical exfoliation process may occur during the synthesis process of PbS QDs, which then partially cover the surface of PbS QDs to form quasi core/shell nanoparticles.

Figure 4 shows absorption and PL spectra of OA-capped PbS, PbS/G, and Cd-doped PbS/G QDs. OA-capped PbS QDs exhibit a well-defined excitonic peak at  $923\text{ nm}$ . This peak becomes broader, quenches, and shifts to the red for PbS/G QDs, which can be caused either by deposition of graphene shell or by their larger crystal size ( $3.5\text{ nm}$  vs  $3.0\text{ nm}$  according to TEM data), or by both these factors. For Cd-doped nanocrystals, the excitonic peak slightly quenches and further shifts to the red, which is beneficial in terms of the improved near-infrared absorption of the solar spectrum. Similar to the absorption spectra, the PL spectrum of PbS/G QDs exhibits a red shift (move to higher wavelengths) and broadening as compared to the OA-capped PbS QDs, while the PL spectrum of Cd-doped nanocrystals has nearly the same spectral width as for the OA-capped PbS QDs, but further shifts to the red. After

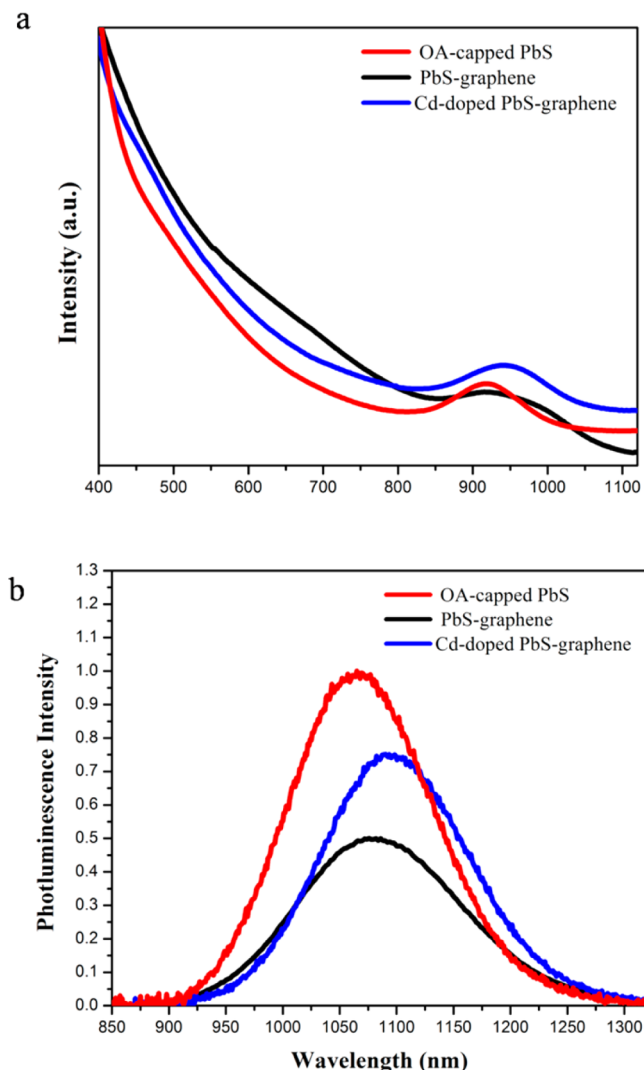


**Figure 4.** Optical properties of hybrid nanocrystals. (a) The absorption spectrum of PbS/G QDs exhibits a red shift compared to the OA-capped PbS QDs prepared at the same condition, particularly when Cd doping was afforded. (b) PL spectra of GQDs on PbS QDs.

doping the surface of PbS/G QD with Cd atoms, the size of quantum dots was increased to some extent as illustrated in Figure S4. As a result, the observed red shift could be attributed to the size effect.

DFT simulations have been conducted in order to determine whether the incomplete passivation of the surface of PbS nanocrystals with graphene sheets would be feasible from energetic point of view, and to compare trap states in PbS and PbS/G QDs. For the PbS QDs, a model of nonpassivated (“naked”) nanocrystal without any ligand shell at the surface was applied (Figure 5a). For quasi core/shell PbS/G QDs, the graphene layers partially covered the surface of the same PbS QD, as illustrated in Figure 5a. Since (111) planes of PbS are lead-rich<sup>39</sup> and have more positive charge, the negatively charged graphene sheets<sup>40–42</sup> have a tendency toward surface passivation of these planes. DFT simulation confirms wrapping of PbS QDs with several layers of graphene, which minimizes the total energy of the system. In order to study the number of graphene sheets on the surface of PbS QD, different configurations of the passivated structure were relaxed

energetically using DFT simulation and the number of graphene sheets versus energy was plotted as shown in Figure S6. The results show that, by using eight graphene sheets, the system could have the lowest energy. The size of graphene sheets was fixed at 2.5 nm according to the TEM results. Figure 5b,c shows the density of states (DOS) of PbS and PbS/G QDs. The conduction bands, valence bands, and Fermi level of PbS QDs are at -3.2, -5.1, and -3.75 eV, respectively. Since no ligand passivation was taken into account in the PbS model, there are naturally trap states appearing within the band gap due to the dangling bonds. Passivation by organic ligands such as OA would greatly reduce the amount of trap states of PbS QDs, as discussed in detail in refs 38 and 43. After passivation of PbS QD with graphene, the Fermi level of the system is decreased to -4.4 eV. This energy level is closer to the TiO<sub>2</sub> Fermi level,<sup>43</sup> and as a result, it is beneficial for transportation of electrons. In addition, the DFT simulation shows that passivation of graphene decreases the amount of midgap states of the PbS QDs (Figure 5c). This is further supported by the time-resolved PL (TRPL) measurements, conducted at 405 nm excitation by monitoring PL decays at wavelengths corresponding to the peaks of steady-state PL spectra of OA-capped PbS, PbS/G, and Cd-doped PbS/G QDs (Figure 5b). Transient PL-intensity profiles were fitted to the stretched decay fits and are shown as solid curves in Figure 5d with the fit parameters illustrated in Table 1. The PL lifetime of PbS/G QDs was 0.78 μs, ~40% shorter than that of the OA-capped PbS QDs (1.2 μs). According to the TRPL results, in the presence of graphene, the electron transfer occurs much faster than the decay of photoexcitations; the recombination of carriers may be significantly hindered. In addition, the highly conductive graphene provides efficient and direct routes for the transportation of the electrons. The efficient transport of the photogenerated carriers enhances the current in the external circuit, which improves the photovoltaic performance.<sup>14</sup> In order to study the role of Cd on the carrier lifetime, the TRPL measurement for the Cd-doped PbS QD (without graphene) was also performed. As seen, the presence of Cd atoms on the surface of PbS QD increases the carrier’s lifetime drastically (1.43 μs) and there is no quenching effect after Cd doping. Also, the PLQY results of the sample remained almost unchanged, i.e., 28% for OA-PbS QDs, 29% for PbS/G QDs, and 30% for Cd doping of PbS/G QDs.

Due to the shorter lifetime of charge carriers in the PbS/G QDs than in other types of QDs, the carriers can reach the electrodes in the solar cell before recombination and therefore higher power conversion efficiency can be expected. We have used OA-capped PbS, MPA-capped PbS, PbS/G, and Cd-doped PbS/G QDs as active layers of bulk heterojunction solar cells, as illustrated in Figure 6a for the example of the PbS QD active layer. The device architecture included the FTO substrate covered with a thin TiO<sub>2</sub> layer (~300 nm) and the QD film (~360 nm). The hole transfer layer (MoO<sub>3</sub>) and the gold contact had thicknesses of about 15 and 100 nm, respectively. Figure 6b shows the current density–voltage (*J*–*V*) curves for three cells under simulated AM1.5G solar irradiation in air. The figures of merit for these cells are summarized in Table 2. The power conversion efficiency (PCE) of the OA-capped PbS QDs was low,  $1.3 \pm 0.1\%$ . The relatively low current density and open voltage of this device is attributed to long capping molecules on QDs which hinder the carrier transport in QD films.<sup>37</sup> For PbS/G and Cd-doped PbS/G QD solar cells, the PCE improved by almost 3 times,

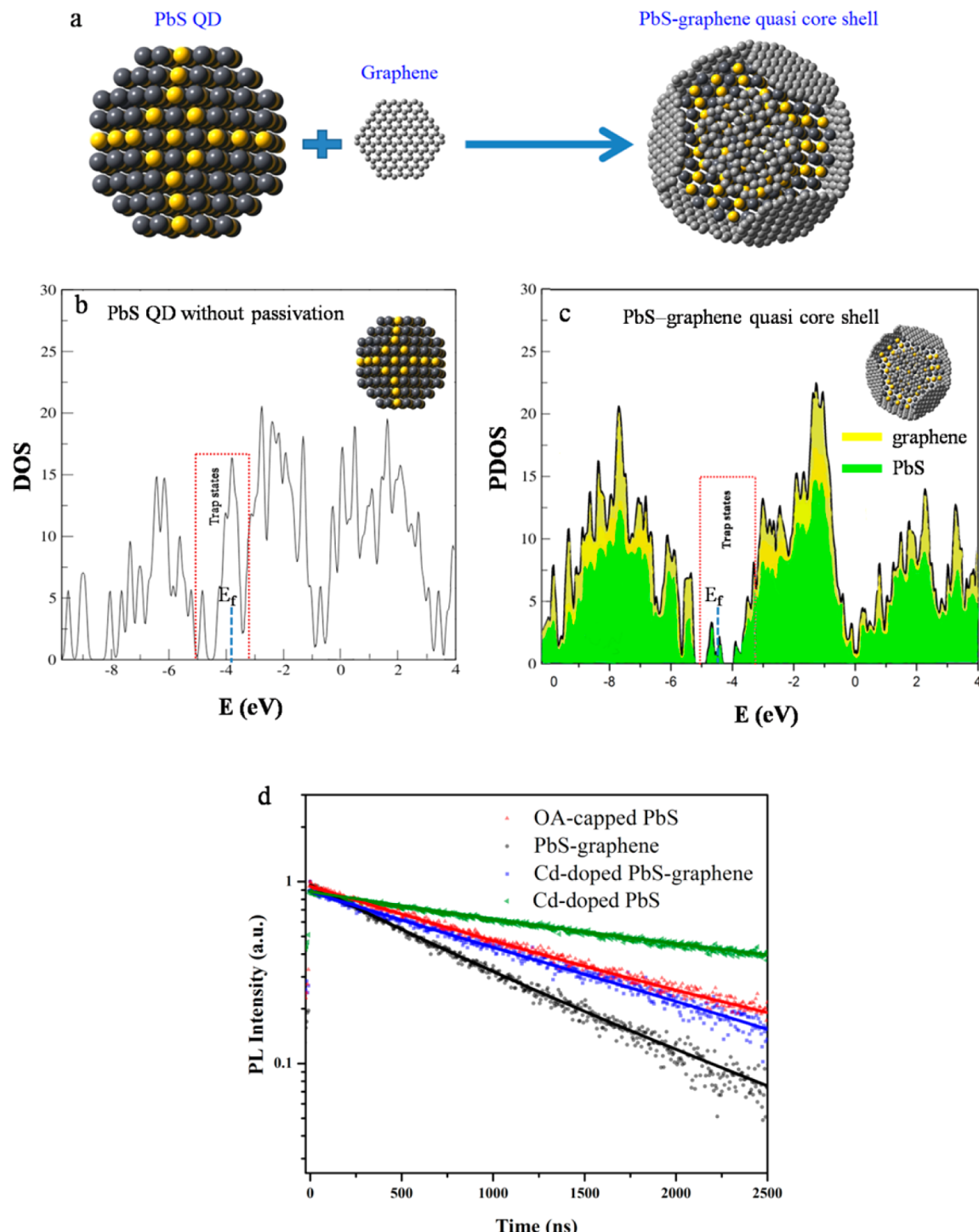


**Figure 5.** (a) Schematic model of PbS and PbS/G QDs used for DFT simulations. Simulations indicate that warping of PbS nanocrystals by a layer of G minimizes the total energy of the system. (b) The electronic structure of PbS QDs contains many midgap trap states due to surface dangling bands. (c) Effect of graphene passivation on the trap states of PbS QDs. (d) PL decay curves of OA-PbS QDs (red), PbS/G QDs (black), and Cd-doped PbS/G (blue) at 405 nm excitation monitored at wavelengths corresponding to peaks of emission spectra in Figure 4b. The curves were fitted to a stretched exponential form (solid lines):  $I(t) = I_0 e^{-(t/\tau)^\beta}$ , where  $\beta$  is a stretch parameter and  $\tau$  is the decay time, with the reduced  $\chi^2 \leq 1.2$ .

reaching  $3.6 \pm 0.3\%$  and  $4.1 \pm 0.2\%$ , respectively. Doping of Cd atoms on the surface of PbS QDs (even in low amounts) was previously illustrated to decrease the trap states and increase the photovoltaic (PV) performance due to the enhancement of fill factor.<sup>43–45</sup> Nevertheless, in PbS/G QDs, the presence of graphene can affect the adsorption of Cd atoms on the surface of PbS QDs during the chemical processing. As a result,

complete passivation of deep trap states could not be attained. The presence of Cd on the surface of graphene could also change its transport properties. Consequently, the current density of Cd-doped PbS/G devices was slightly lower than that of undoped PbS/G QDs. In order to further study the role of graphene passivation, Cd-doped PbS QD solar cell was also fabricated. The result of PV measurement demonstrates that

**Table 1.** Fitting Parameters of the Corresponding PL Decay Curves

sample	$\tau$ ( $\mu$ s)	$\beta$	$\chi$
OA-capped PbS QDs	1.2	0.83	1.07
PbS/G QDs	0.782	0.91	1.04
Cd-doped PbS/G QDs	1.1	0.85	1.06
Cd-doped PbS QDs	1.43	0.79	1.09

Cd doping enhances the current density and fill factor (FF) of the device compared with the OA-capped PbS QD solar cell. In the case of graphene passivation (without Cd doping), the current density is improved by 50% but the FF is reduced by 17%. Therefore, by simultaneous graphene passivation and Cd doping, both  $J_{sc}$  and FF are improved and a higher PV performance is attained. In addition, MPA molecules were also used as short passivation ligands. Solar cell devices were fabricated based on MPA-capped PbS QDs using the solid-state ligand exchange method. As shown in Figure 6a, the devices show on average a PCE of  $3.3 \pm 0.1\%$ . The lower  $J_{sc}$  of the devices compared with the graphene-based cells is noticeable. Figure 6c shows the external quantum efficiency (EQE) spectra of the OA-capped PbS, MPA-capped PbS QDs, PbS/G QD, Cd-doped PbS/G QD, and Cd-doped PbS QD solar cells, which are in good agreement with  $J-V$  measurements. The generation of photocurrent starts at  $\sim 1000$  nm for the PbS/G cell, which is in agreement with the band gap of this material determined from the optical absorption spectrum (Figure 4a). Based on the experimental results, we could conclude that the

**Table 2.** Figures of Merit for the Solar Cell Devices Using Different QD Materials as an Active Layer

active layer	$V_{oc}$ (V)	$J_{sc}$ ( $\text{mA}/\text{cm}^2$ )	FF (%)	PCE (%)
OA-capped PbS QDs	$0.48 \pm 0.07$	$6.2 \pm 1.8$	$45 \pm 4$	$1.3 \pm 0.1$
MPA-capped PbS QDs	$0.57 \pm 0.04$	$11.1 \pm 1.3$	$53 \pm 3$	$3.3 \pm 0.1$
PbS/G QDs	$0.58 \pm 0.03$	$13.4 \pm 1.1$	$47 \pm 5$	$3.6 \pm 0.3$
Cd-doped PbS/G QDs	$0.59 \pm 0.04$	$12.3 \pm 1.2$	$56 \pm 3$	$4.1 \pm 0.2$
Cd-doped PbS QDs	$0.59 \pm 0.03$	$8.8 \pm 1.1$	$57 \pm 3$	$2.96 \pm 0.2$

most important role of graphene in the solar cell device is fast extraction of carriers due to the improvement of incident photon-to-current efficiency (IPCE) and  $J_{sc}$ . DFT simulation also supports the effect of ultrathin graphene coating on the passivation of the trap states, which reduces recombination of carriers.

#### 4. CONCLUSIONS

We introduced a hot-injection procedure to synthesize monodisperse, highly crystalline PbS/G QDs with an average size of 3.5 nm. As illustrated by DFT calculation, the surface passivation of PbS QDs by graphene results in a decrease of the midgap states. Time-resolved PL measurements further revealed that PbS/G QDs have a shorter PL lifetime ( $0.78 \mu\text{s}$ ) than OA-capped PbS QDs ( $1.2 \mu\text{s}$ ) due to the fast

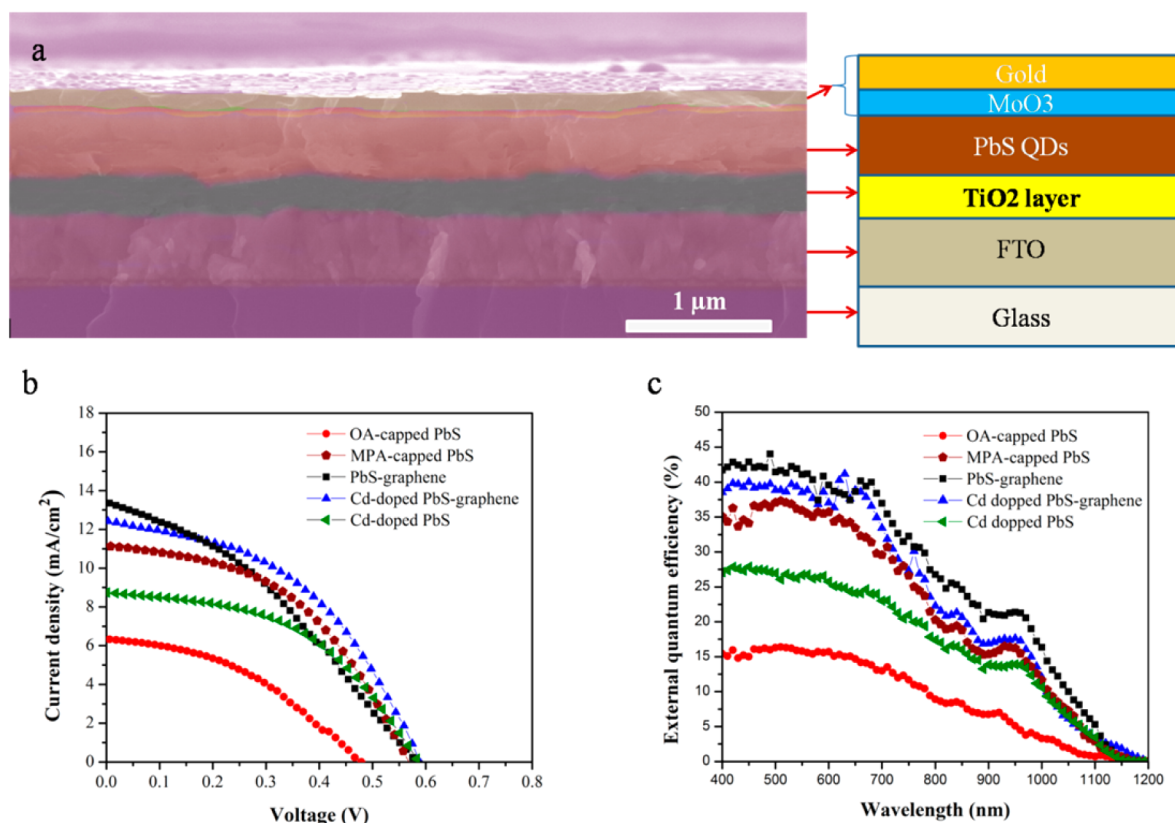


**Figure 6.** Characteristics of bulk heterojunction PbS/G CQD solar cells. (a) Cross-sectional SEM image shows the structure of the fabricated devices. The absorption layer was oleic acid–PbS QDs and PbS/G QDs with  $\sim 360$  nm thickness. (b)  $J-V$  curves under AM1.5G indicate the photovoltaic performance of the heterojunction devices. (c) EQE spectra determine the effect of graphene passivation and Cd doping on the quantum efficiency of the PbS CQD films.

extraction of the carriers. These favorable characteristics of PbS/G QDs allowed us to use them as active layers of solar cells with an efficiency of 3.6%, which could be further improved to 4.1% by Cd doping. Our study demonstrates the importance of proper heterostructure design of hybrid materials for photovoltaic applications.

## ■ ASSOCIATED CONTENT

### Supporting Information

The Supporting Information is available free of charge on the ACS Publications website at DOI: [10.1021/acs.jpcc.Sb04195](https://doi.org/10.1021/acs.jpcc.Sb04195).

HRTEM images and EDS analysis of graphene QDs and PbS QDs; XPS analysis of GO and PbS/G; total energy vs number of graphene sheets for PbS QDs ([PDF](#))

## ■ AUTHOR INFORMATION

### Corresponding Author

\*E-mail: [simchi@sharif.edu](mailto:simchi@sharif.edu). Tel.: +98 (21) 6616 5261. Fax: +98 (21) 6600 5717.

### Notes

The authors declare no competing financial interest.

## ■ ACKNOWLEDGMENTS

This work was supported by the General Research Fund (Project 612113) from the Hong Kong Research Grant Council, by the Hong Kong Innovation and Technology Fund (Project ITS/117/13) from the Innovation and Technology Commission, and by the Specialized Research Fund for the Doctoral Program of Higher Education (SRFDP) and Research Grants Council Earmarked Research Grants (RGC-ERG) under the grant M\_CityU 102/12. A.S. also thanks the Grant Program of Sharif University of Technology (No. G930305) and Elite National Institute for funding support. The contribution of Prof. Andrey L. Rogach through scientific discussions and manuscript preparation is highly appreciated.

## ■ REFERENCES

- (1) Kim, J. Y.; Voznyy, O.; Zhitomirsky, D.; Sargent, E. H. 25th Anniversary Article: Colloidal Quantum Dot Materials and Devices: A Quarter-Century of Advances. *Adv. Mater.* **2013**, *25*, 4986–5010.
- (2) Kershaw, S. V.; Susha, A. S.; Rogach, A. L. Narrow Bandgap Colloidal Metal Chalcogenide Quantum Dots: Synthetic Methods, Heterostructures, Assemblies, Electronic and Infrared Optical Properties. *Chem. Soc. Rev.* **2013**, *42*, 3033–3087.
- (3) Shirasaki, Y.; Supran, G. J.; Bawendi, M. G.; Bulović, V. Emergence of Colloidal Quantum-Dot Light-Emitting Technologies. *Nat. Photonics* **2013**, *7*, 13–23.
- (4) Hines, M. A.; Scholes, G. D. Colloidal PbS Nanocrystals With Size-Tunable Near-Infrared Emission: Observation of Post-Synthesis Self-Narrowing of The Particle Size Distribution. *Adv. Mater.* **2003**, *15*, 1844–1849.
- (5) McDonald, S. A.; Konstantatos, G.; Zhang, S.; Cyr, P. W.; Klem, E. J.; Levina, L.; Sargent, E. H. Solution-Processed PbS Quantum Dot Infrared Photodetectors and Photovoltaics. *Nat. Mater.* **2005**, *4*, 138–142.
- (6) Yu, D.; Wang, C.; Guyot-Sionnest, P. n-Type Conducting CdSe Nanocrystal Solids. *Science* **2003**, *300*, 1277–1280.
- (7) Hetsch, F.; Zhao, N.; Kershaw, S. V.; Rogach, A. L. Quantum Dot Field Effect Transistors. *Mater. Today* **2013**, *16*, 312–325.
- (8) Gao, J.; Johnson, J. C. Charge Trapping in Bright and Dark States of Coupled PbS Quantum Dot Films. *ACS Nano* **2012**, *6*, 3292–3303.
- (9) Luther, J. M.; Law, M.; Song, Q.; Perkins, C. L.; Beard, M. C.; Nozik, A. J. Structural, Optical, and Electrical Properties of Self-Assembled Films of PbSe Nanocrystals Treated with 1,2-Ethanedithiol. *ACS Nano* **2008**, *2*, 271–280.
- (10) Liu, Y.; Gibbs, M.; Puthussery, J.; Gaik, S.; Ihly, R.; Hillhouse, H. W.; Law, M. Dependence of Carrier Mobility on Nanocrystal Size and Ligand Length in PbSe Nanocrystal Solids. *Nano Lett.* **2010**, *10*, 1960–1969.
- (11) Zhitomirsky, D.; Voznyy, O.; Levina, L.; Hoogland, S.; Kemp, K. W.; Ip, A. H.; Thon, S. M.; Sargent, E. H. Engineering Colloidal Quantum Dot Solids Within and Beyond the Mobility-Invariant Regime. *Nat. Commun.* **2014**, *5*, 3803–3808.
- (12) Ning, Z.; Zhitomirsky, D.; Adinolfi, V.; Sutherland, B.; Xu, J.; Voznyy, O.; Maraghechi, P.; Lan, X.; Hoogland, S.; Ren, Y.; et al. Graded Doping for Enhanced Colloidal Quantum Dot Photovoltaics. *Adv. Mater.* **2013**, *25*, 1719–1723.
- (13) Tavakoli, M. M.; Simchi, A.; Aashuri, H. Supercritical Synthesis and in Situ Deposition of PbS Nanocrystals With Oleic Acid Passivation for Quantum Dot Solar Cells. *Mater. Chem. Phys.* **2015**, *156*, 163–169.
- (14) Tang, J.; Liu, H.; Zhitomirsky, D.; Hoogland, S.; Wang, X.; Furukawa, M.; Levina, L.; Sargent, E. H. Quantum Junction Solar Cells. *Nano Lett.* **2012**, *12*, 4889–4894.
- (15) Ning, Z.; Voznyy, O.; Pan, J.; Hoogland, S.; Adinolfi, V.; Xu, J.; Li, M.; Kirmani, A. R.; Sun, J.; Minor, J.; et al. Air-Stable n-type Colloidal Quantum Dot Solids. *Nat. Mater.* **2014**, *13*, 822–828.
- (16) Chuang, C. M.; Brown, P. R.; Bulovic, V.; Bawendi, M. G. Improved Performance and Stability in Quantum Dot Solar Cells Through Band Alignment Engineering. *Nat. Mater.* **2014**, *13*, 796–801.
- (17) Novoselov, K. S.; Geim, A. K.; Morozov, S. V.; Jiang, D.; Zhang, Y.; Dubonos, S. V.; Grigorieva, I. V.; Firsov, A. A. Electric Field Effect in Atomically Thin Carbon Films. *Science* **2004**, *306*, 666–669.
- (18) Avouris, P.; Chen, Z.; Perebeinos, V. Carbon-Based Electronics. *Nat. Nanotechnol.* **2007**, *2*, 605–615.
- (19) Yong, V.; Tour, J. M. Theoretical Efficiency of Graphene-Based Photovoltaics. *Small* **2010**, *6*, 313–318.
- (20) Geim, A. K.; Novoselov, K. S. The Rise of Graphene. *Nat. Mater.* **2007**, *6*, 183–191.
- (21) Chae, H. K.; Siberio-Pérez, D. Y.; Kim, J.; Go, Y.; Eddaudi, M.; Matzger, A. J.; O'Keeffe, M.; Yaghi, O. M. A Route to High Surface Area, Porosity and Inclusion of Large Molecules in Crystals. *Nature* **2004**, *427*, 523–527.
- (22) Freitag, M.; Steiner, M.; Martin, Y.; Perebeinos, V.; Chen, Z.; Tsang, J. C.; Avouris, P. Energy Dissipation in Graphene Field-Effect Transistors. *Nano Lett.* **2009**, *9*, 1883–1888.
- (23) Stampfer, C.; Schurtenberger, E.; Molitor, F.; Guttinger, J.; Ihn, T.; Ensslin, K. Tunable Graphene Single Electron Transistor. *Nano Lett.* **2008**, *8*, 2378–2383.
- (24) Stoller, M. D.; Park, S.; Zhu, Y.; An, J.; Ruoff, R. S. Graphene-Based Ultracapacitors. *Nano Lett.* **2008**, *8*, 3498–3502.
- (25) Ang, P. K.; Chen, W.; Wee, A. T. S.; Loh, K. P. Solution-Gated Epitaxial Graphene as PH Sensor. *J. Am. Chem. Soc.* **2008**, *130*, 14392–14393.
- (26) Zhou, M.; Zhai, Y. M.; Dong, S. J. Electrochemical Sensing and Biosensing Platform Based on Chemically Reduced Graphene Oxide. *Anal. Chem.* **2009**, *81*, 5603–5613.
- (27) Zhang, D.; Gan, L.; Cao, Y.; Wang, Q.; Qi, L.; Guo, X. Understanding Charge Transfer at PbS-Decorated Graphene Surfaces toward a Tunable Photosensor. *Adv. Mater.* **2012**, *24*, 2715–2720.
- (28) Eck, M.; Van Pham, C.; Züfle, S.; Neukom, M.; Sessler, M.; Scheunemann, D.; Erdem, E.; Weber, S.; Borchert, H.; Ruhstaller, B.; et al. Improved Efficiency of Bulk Heterojunction Hybrid Solar Cells by Utilizing CdSe Quantum Dot–Graphene Nanocomposites. *Phys. Chem. Chem. Phys.* **2014**, *16*, 12251–12260.
- (29) Cuong, T. V.; Pham, V. H.; Chung, J. S.; Shin, E. W.; Yoo, D. H.; Hahn, S. H.; Kohl, P. A.; Huh, J. S.; Rue, G. H.; Kim, E. J.; Hur, S. H.; Kohl, P. A. Solution-Processed ZnO-Chemically Converted Graphene Gas Sensor. *Mater. Lett.* **2010**, *64*, 2479–2482.
- (30) Zhang, Y.; Tang, Z.-R.; Fu, X.; Xu, Y.-J. TiO<sub>2</sub>–Graphene Nanocomposites for Gas-Phase Photocatalytic Degradation of Volatile

Aromatic Pollutant: Is TiO<sub>2</sub>—Graphene Truly Different from Other TiO<sub>2</sub>–Carbon Composite Materials. *ACS Nano* **2010**, *4*, 7303–7314.

(31) Tayyebi, A.; Tavakoli, M. M.; Outokesh, M.; Shafeekhani, A.; Simchi, A. Supercritical Synthesis and Characterization of “Graphene-PbS Quantum Dots” Composite with Enhanced Photovoltaic Properties. *Ind. Eng. Chem. Res.* **2015**, DOI: 10.1021/acs.iecr.5b00008.

(32) Konstantatos, G.; Badioli, M.; Gaudreau, L.; Osmond, J.; Bernechea, M.; de Arquer, F. P. G.; Koppens, F. H.; Gatti, F. Hybrid Graphene-Quantum Dot Phototransistors with Ultrahigh Gain. *Nat. Nanotechnol.* **2012**, *7*, 363–368.

(33) Huang, Y. Q.; Zhu, R. J.; Kang, N.; Du, J.; Xu, H. Q. Photoelectrical Response of Hybrid Graphene-PbS Quantum Dot Devices. *Appl. Phys. Lett.* **2013**, *103*, 143119.

(34) Parand, P.; Samadpour, M.; Esfandiar, A.; Iraji Zad, A. Graphene/PbS as a Novel Counter Electrode for Quantum Dot Sensitized Solar Cells. *ACS Photonics* **2014**, *1*, 323–330.

(35) Zhang, M.; Bai, L.; Shang, W.; Xie, W.; Ma, H.; Fu, Y.; Yang, S.; et al. Facile Synthesis of Water-Soluble, Highly Fluorescent Graphene Quantum Dots as a Robust Biological Label for Stem Cells. *J. Mater. Chem.* **2012**, *22*, 7461–7467.

(36) Nursanto, E. B.; Nugroho, A.; Hong, S. A.; Kim, S. J.; Chung, K. Y.; Kim, J. Facile Synthesis of Reduced Graphene Oxide in Supercritical Alcohols and its Lithium Storage Capacity. *Green Chem.* **2011**, *13*, 2714–2718.

(37) Burschka, J.; Pellet, N.; Moon, S.-J.; Humphry-Baker, R.; Gao, P.; Nazeeruddin, M. K.; Grätzel, M. Sequential Deposition as a Route to High-performance Perovskite-sensitized Solar Cells. *Nature* **2013**, *499*, 316–319.

(38) Tavakoli, M. M.; Tayyebi, A.; Simchi, A.; Aashuri, H.; Outokesh, M.; Fan, Z. Physicochemical Properties of Hybrid Graphene-Lead Sulfide Quantum Dots Prepared by Supercritical Ethanol. *J. Nanopart. Res.* **2015**, *17*, 1–13.

(39) Voznyy, O.; Thon, S. M.; Ip, A. H.; Sargent, E. H. Dynamic Trap Formation and Elimination in Colloidal Quantum Dots. *J. Phys. Chem. Lett.* **2013**, *4*, 987–992.

(40) Niyogi, S.; Bekyarova, E.; Itkis, M. E.; McWilliams, J. L.; Hamon, M. A.; Haddon, R. C. Solution Properties of Graphite and Graphene. *J. Am. Chem. Soc.* **2006**, *128*, 7720–7721.

(41) Tavakoli, M. M.; Tavakoli, R.; Davami, P.; Aashuri, H. A Quantitative Approach to Study Solid State Phase Coarsening in Solder Alloys Using Combined Phase-Field Modeling and Experimental Observation. *J. Comput. Electron.* **2014**, *13*, 425–431.

(42) Tavakkoli, M. M.; Abbasi, S. M. Effect of Molybdenum on Grain Boundary Segregation in Incoloy 901 Superalloy. *Mater. Eng.* **2013**, *46*, 573–578.

(43) Ip, A. H.; Thon, S. M.; Hoogland, S.; Voznyy, O.; Zhitomirsky, D.; Debnath, R.; Levina, L.; et al. Hybrid Passivated Colloidal Quantum Dot Solids. *Nat. Nanotechnol.* **2012**, *7*, 577–582.

(44) Gao, Y.; Jin, H.; Lin, Q.; Li, X.; Tavakoli, M. M.; Leung, S.; Tang, W. M.; Zhou, L.; Chan, H. L.; Fan, Z. Highly Flexible and Transferable Supercapacitors with Ordered Three-Dimensional MnO<sub>2</sub>/Au/MnO<sub>2</sub> Nanospike Arrays. *J. Mater. Chem. A* **2015**, *3*, 10199–10204.

(45) Son, D. I.; Kwon, B. W.; Park, D. H.; Seo, W. S.; Yi, Y.; Angadi, B.; Choi, W. K.; Lee, C.-L. Emissive ZnO-Graphene Quantum Dots for White-Light-Emitting Diodes. *Nat. Nanotechnol.* **2012**, *7*, 465–471.